Critical impact of nitrogen vacancies in nonradical carbocatalysis on nitrogen-doped graphitic biochar

Zhonghao Wan[1], Zibo Xu[1], Yuqing Sun[1], Mingjing He[1], Deyi Hou[2], Xinde Cao[3], Daniel C.W. Tsang[1, *]

[1] Department of Civil and Environmental Engineering, The Hong Kong Polytechnic University, Hung Hom, Kowloon, Hong Kong, China.

[2] School of Environment, Tsinghua University, Beijing 100084, China.

[3] School of Environmental Science and Engineering, Shanghai Jiao Tong University, 800 Dongchuan Road, Shanghai 200240, China.

* Corresponding author: dan.tsang@polyu.edu.hk

ABSTRACT: Nitrogen-doped graphitic biochar (NBC) has boosted the development of nonradical peroxymonosulfate (PMS) activation in environmental remediation. However, the specific role of nitrogen species played in NBC-based nonradical carbocatalysis remains vaguely interpreted. To pinpoint the critical nitrogen speciation, a sophisticated thermo-mechanochemical manipulation was exploited to prepare a series of NBCs with similar dimensional structure and oxygen level but different nitrogen species (*i.e.*, dopants and vacancies). Different from conventional perspectives, the nonradical NBC-based carbocatalysis was found to be preferably determined by the nitrogen vacancies more than their parent nitrogen dopants. Raman depth analysis evidenced that a complete transformation of nitrogen dopants into nitrogen vacancies could be achieved at 800 ℃, whereby an excellent nonradical abatement of 4-chlorophenol (4-CH, 90.9% removal) was found for the NBC800 with a low PMS consumption (1.24 mM). According to PMS adsorption experiments, nitrogen vacancies exhibited the highest affinity towards the PMS molecules compared to nitrogen dopants, which accounted for the superior carbocatalysis. Electron paramagnetic resonance (EPR) and Raman spectroscopic analyses indicated that the original PMS molecules were bound to positively-charged nitrogen vacancies, and the robust metastable complex ($*HSO_5^-$) evolved subsequently *via* the hydrogen abstraction by adjacent persistent free radicals (PFRs). *In-situ* Raman techniques could be adopted to estimate the level of nitrogen vacancies associated with the polarization of electron distribution. The flexible feature and practical prospect of nitrogen vacancy based carbocatalysis were also testified in the remediation of simulated phenolic industrial wastewater. Overall, this study unravels the dilemma in the current NBC-based nonradical carbocatalysis and advances our understanding of nitrogen doping technology for next-generation biochar design.

INTRODUCTION

Carbonaceous catalysts is of great interest for the environmental community as they can trigger nonradical peroxymonosulfate (PMS) activation for organic remediation, which can help to reduce the chemical input and avoid the generation of highly halogenated intermediates.[1-3] In principle, the primary reason to study nonradical carbocatalysis is that it can alleviate the severe surface corrosion of carbons encountered in radical-based carbocatalysis, thus fostering practical environmental application. Conventionally, transition metals were incorporated within the carbon matrix to promote their catalytic performance.[4] However, inevitable metal leaching in the metal-involved systems may cause secondary pollution, and the nonradical regime on metal catalysts remains debatable and is limited to only a few transition metals (*e.g.*, Cu, Mn).[5, 6] Metal-free technology rises as a game-changer to modify carbon configuration and inherent electroactive components, thus rendering nonradical carbocatalysts a comparable or even better efficacy than those of metal-based catalysts.[7]

Heteroatoms doping refers to a technique to incorporate various earth-abundant non-metallic elements (*e.g.*, nitrogen (N), sulphur (S), and boron (B)) into the hexagonal framework of well-ordered crystalline carbon network.[8] The nitrogen doping technology, which has the highest efficacy over others, has been extensively explored to facilitate the catalysis of carbonaceous materials (graphene,[9, 10] carbon nanotubes (CNTs),[11] activated carbon (AC),[12] *etc.*) in the nonradical carbocatalysis. Theoretically, the incorporated nitrogen dopants (*i.e.*, pyrrolic N, pyridinic N, and graphitic N) can either enrich the surface charge density or afford the adjacent carbon atoms a robust affinity toward peroxide bond, reducing its energy threshold to generate reactive oxygen species (ROS) bound onto the surface.[13-15]

Recent studies have attempted to explore the mechanistic roles of nitrogen played in the nonradical peroxide activation. Ren et al. revealed the intrinsic nature of PMS activation on the

nitrogen-doped CNTs (NCNTs), where electrochemical methods verified that the formation of surface-bound metastable complex (NCNTs-PMS*) with a high chemical potential boosted the nonradical organic oxidation.[16] Graphitic N with a strong affinity towards the PMS was considered as the dominant active sites on the NCNTs. However, the nonradical mechanisms on the low-dimensional nanocarbons such as NCNTs may not represent the high-dimensional carbocatalysts (*e.g.*, graphitic biochar) that possess more complicated structures. Besides, the high synthesis cost and the critical requirements for material quality currently impede the further upscaling application of lower-dimensional carbocatalysts from a sustainable perspective.[17]

Compared with those costly low-dimensional nanocarbons, graphitic biochar shows great advantages owing to its abundant availability and readily maneuverable feature, making it an economically and industrially attractive carbocatalyst.[18, 19] Zhu et al. first fabricated nitrogen-doped graphitic biochar (NBC) using lignocellulosic biomass and reported the nonradical persulfate activation.[20] Subsequently, Ho et al. showed the existence of surface reactive complex on the NBC similar to that on the NCNTs.[21] Intriguingly, debatable perspectives remain over the origin of surface metastable complex on the NBC. The above studies regarded graphitic N as the critical active sites, [20] while Wang et al. suggested that edge nitrogen species (pyrrolic N and pyridinic N) should determine the formation of surface reactive complex on the NBC.[18] Currently, the existing theoretical basis was constructed on a simplified modelling with density functional theory (DFT) which adopted hexagonal units to roughly represent the complicated biochar structure, and the disagreements were heavily placed on the scavenger experiments whose credibility was questionable in the biochar-based systems.[2, 15] Further investigation and more detailed information are essential for improving the long-term development of biochar.

Especially, the critical nitrogen speciation needs to be clarified in the nonradical NBC-based

carbocatalysis. The correlation between the nonradical surface complex and the nitrogen speciation on NBC is still vaguely unveiled. Most of the studies found it hard to interpret the contradictory phenomenon that a lower nitrogen level subject to a higher treatment temperature would lead to a better catalytic performance.[22-24] With respect to low-dimensional nanocarbons, this could be attributed to the decomposition of nitrogen dopants which creates more structural defects to disrupt the spin and electronic order of carbon units.[25] However, raw NBC presents mediocre activity despite its high original defective level.[26] It is noteworthy that, in the case of carbon nitride, the nitrogen vacancies can enhance the catalytic activity by increasing the polarization of electron distribution.[27, 28] Nevertheless, little information is available regarding potential correlation between the nonradical surface complex and nitrogen vacancies.

To scrutinize the critical roles of nitrogen dopants and vacancies in the emerging biochar-based carbocatalysis, we fabricated a series of NBCs with similar original defective and oxygen levels. Mechanochemical ball milling was employed as a mild surface doping process with ammonia as the nitrogen precursor. We hypothesized that the temperature-oriented annealing could readily regulate the nitrogen species in a sequential order, *i.e.*, amino-N-dominated (< 500 °C), pyrrolic- and pyridinic-N-dominated (500−700 °C), graphitic-N-dominated (700−800 °C) types, and nitrogen vacancies (800 °C). With multiple characterization and experimental manners including Raman spectroscopy, electron paramagnetic resonance (EPR), substrate specificity analysis, *etc.*, we proposed that the evolved nitrogen vacancies at 800 °C can launch the adjacent persistent free radicals (PFRs) to abstract hydrogen from the adsorbed PMS molecules, leading to the formation of surface-confined metastable complex (*HSO_5^-). Overall, this work clarified the critical nitrogen speciation in the NBC-based nonradical carbocatalysis for advancing future biochar design.

MATERIALS AND METHODS

Chemicals. All chemicals present in this study were of analytical reagent grade. Detailed information can be found in Supporting Information (**Text S1**).

Preparation of Biochars with Tailored Defective and Nitrogen Doping Level. Raw lignocellulosic biomass with a low ash content, namely oak tree sawdust (N < 1 *wt.*%), was collected from Hubei, China without further acid washing. The sawdust was pulverized to pass through a 120-mesh sieve (particle size < 0.125 mm) and dried under 105 ℃ prior to the thermal treatment. The benchmark, defective biochar (DBC), was prepared according to the method reported in our previous studies,[26, 29] where 20 g raw biomass solids were placed in a corundum jar and transferred into a tubular reactor. Under CO_2 purging (100 mL min^{-1}), pyrolysis proceeded at 800 ℃ for 2 h with a ramping rate of 5 ℃ min^{-1}. The high pyrolytic temperature at 800 ℃ could remove all the labile electroactive components that may cause interference with the subsequent ROS identification. Rich defects could be guaranteed over the reaction between carbon matrix and CO_2 (Boudouard reaction: $C + CO_2 \rightarrow 2CO$, temperature > 720 ℃) to accommodate heteroatoms. Wet ball milling as a powerful non-equilibrium processing method was adopted to tailor the nitrogen-doping level using $NH_3 \bullet H_2O$ as both reductive agent and nitrogen additive.[30] Specifically, 2 g DBC was contained in a 300 mL Teflon jar with 100 g corundum balls (uniform ball diameter distribution of 1−3 mm). Then, 20 mL $NH_3 \bullet H_2O$ was slowly transferred into a jar under nitrogen purging prior to its seal and placement in a planetary ball mill machine (Changsha Deke Instrument Equipment Co., Ltd., China). The ball milling speed and duration time were set at 600 rpm and 12 h, respectively, and the rotation direction was automatically altered every 15 min to avoid solid deposition. The ball-milled DBC, denoted as the BMDBC, was dried at 60 ℃ overnight and then annealed under different temperatures (*i.e.*, 500, 600, 700, and 800 ℃ with a ramping rate of 5 ℃

130 min^{-1}) for 1 h in N_2 environment (100 mL min^{-1}) to tune the nitrogenous species. The resultant
131 biochars were denoted as the NBCX, where X indicates the annealing temperature. Preparation of
132 several counterpart nitrogen-doped carbons was also conducted. The CNTs, graphite (GR), and
133 AC were chosen as the representative carbonaceous controls with different dimensional structures
134 (*i.e.*, 1D CNTs, 2.5D GR, and 3D AC, respectively).[31] The nitrogen-doped GR and AC were
135 prepared following the same procedure to that of the NBCs, labelled as NG and NAC, respectively.
136 To maintain the original tunnel structure of CNTs, the conventional doping process was selected
137 to prepare the NCNTs (**Text S2**).[16] The NCNTs, NGR, and NAC correspond to the nitrogen-doped
138 carbon which possesses a lower dimension but similar defective and oxygen levels, a similar
139 dimension despite much lower defect and oxygen moieties, and a comparable
140 dimensional/defective structure except for its lower oxygen moieties compared with the NBCs,
141 respectively, which serve to discern the contribution of respective electroactive components.
142 **Characterization.** The detailed information about transmission electron microscopy (TEM,
143 JEOL 2100F, Japan), Raman spectroscopy (Renishaw, UK), thermogravimetric analysis (TG,
144 Rigaku Thermo Plus), X-ray photoelectron spectroscopy (XPS, Thermo Fisher Scientific, USA),
145 *etc*. can be referred to **Text S3**. The EPR (Bruker, Germany) analysis was performed with different
146 spin-trapping agents including 5,5-dimethyl-1-pyrrolidine N−Oxide (DMPO) and 2,2,6,6-
147 tetramethyl-4-piperidone (TEMP), and the specific experimental conditions are described in **Text**
148 **S4**.
149 **Activity Evaluation and Analytical Methods.** The catalytic activity of all the biochar samples
150 was assessed in batch experiments using Oxone ($2KHSO_5 \cdot KHSO_4 \cdot K_2SO_4$, PMS precursor) as an
151 oxidant in aqueous solution. Ubiquitous refractory phenolic organic pollutants omnipresent in
152 industrial wastewater, which possess distinct electrochemical properties,[32] were applied to

evaluate the nonradical carbocatalysis of the NBCs. Specifically, 100 mL solution containing a specific amount of pollutant (*e.g.*, 100 mg L^{-1}, corresponding to the industrial wastewater containing phenolic compounds ranging from 20 to 1200 mg L^{-1}) was put in a 250 mL conical flask covered with foil. Subsequently, 500 mg L^{-1} biochar and 1 g L^{-1} Oxone powder (equivalent to 3.25 mM PMS) were added to initiate the reaction. All experiments were conducted at 25 ±1 ℃ with vigorous stirring at 200 rpm in an oscillator without light irradiation. Further information on the experimental protocol, analytical parameters for different organics, residual PMS, total carbon (TC) consisting of total organic carbon (TOC) and inorganic carbon (IC), *in-situ* Raman Analysis, *etc.* are available in **Text S5**, **Text S6**, and **Text S7**, respectively.

Practical prospects. The durability of the selected NBC was evaluated based on a natural aging process (**Text S8**), which was similar to the pilot-scale production and storage of aged biochar in Kadoorie Farm, Hong Kong.[33] Recyclability test and regeneration of spent biochar were implemented following a protocol reported in our previous work (**Text S8**).[19] To evaluate the catalytic performance under field-relevant conditions, humic acid (HA) and several ubiquitous ions (*i.e.*, Cl^-, CO_3^{2-}, and HCO_3^-) were added as proxy of natural organic matter and background ions, respectively. The compositions of industrial phenolic wastewater were based on the previous reports (**Table S7**),[34-36] and the measurement protocols are described in **Text S9**.

RESULTS AND DISCUSSION

Textural Characteristics of the NBCs. The SEM images in **Figure S1** show that the original biochar produced from lignocellulosic biomass possessed a typical honeycomb structure with well-developed macroporous feature. After ball milling, the BMDBC exhibited a disparate morphology from that of the original DBC with a smaller average size, lower macroporosity, and smoother

surface (**Figure S1b**). Specific surface area (SSA) of the BMDBC decreased to 246 m^2 g^{-1} compared with 366 m^2 g^{-1} for the DBC, which might result from the collapse of porous structure as the total pore volume (V_{total}) decreased from 0.27 to 0.17 cm^3 g^{-1} (**Table S1**). This phenomenon was also ascribed to the coverage of excessive nitrogenous contents. After the annealing process between 500 and 800 ℃, small improvements in the SSA (from 353 to 395 m^2 g^{-1}) and the porosity (from 0.28 to 0.31 cm^3 g^{-1}) were observed owing to the thermal cracking of nitrogen functionalities to evolve open-up pores.[37] The micropore area (from 288 to 167 m^2 g^{-1}) and micropore volume (from 0.15 to 0.09 cm^3 g^{-1}) followed a deceasing trend with the increasing annealing temperature, which was in alignment with the nitrogen adsorption-desorption isotherm curves where the type-IV hysteresis loops moved upwards to a relatively higher P/P_0 region (**Figure S2**). It is expected that the textural properties of biochar matrices maintained stable because the subsequent annealing temperature did not exceed the pyrolytic temperature of original DBC (800 ℃), while the slight decrease in SSA along temperature increase might be due to the disorientation and corrugation of graphitic basal planes during thermal treatment.[9] The increased average pore diameter (D_p) from 2.91 to 3.59 nm and a higher mesoporous density of NBC800 (**Figure S3**) corroborated that a high annealing temperature at 800 ℃ led to a gradual transformation of micropores into mesopores.[20, 22]

Transition of Surface Functionalities into Dopants. Elemental changes of the biochars after ball milling were unveiled using elemental analyser (**Figure S4**). Both carbon and oxygen levels showed a slight change after ball milling with NH_3•H_2O, while the overall nitrogen content significantly elevated from 0.04 to 0.8 *wt.*% (a 20-fold increase), indicating the successful introduction of nitrogen contents. The annealing process at 500 ℃ enriched the carbon level by 5.44 *wt.*% and simultaneously decreased the oxygen level by 4.95 *wt.*%. This phenomenon might

result from the removal of labile surface oxygen contents that had been introduced during the wet ball milling.[38, 39] With the increase of annealing temperature, the nitrogen element experienced a severe loss and declined to 0.23 *wt.*% for the NBC800 due to the weak thermodynamic stability of nitrogenous contents, while its oxygen level progressively increased to 6.24 *wt.*% due to the higher stability of ketonic −C=O.[26, 40] Preservation of the ketonic −C=O was also confirmed in FTIR curves (**Figure S5**), where the characteristic peak at 1623 cm^{-1} assigned to the ketonic −C=O persisted irrespective of the temperature elevation. Other characteristic peaks including the aromatic −C=C or −C−H out of plane deformation at 886 cm^{-1} and the amino groups at ~3500 cm^{-1} could be found in all biochars after nitrogen doping, while the −C=N peak located at 1498 cm^{-1} could only be detected when the annealing temperature was higher than 600 ℃. The decreased intensity of the amino groups and the formation of −C=N over 600 ℃ implied the plausible transformation of amino functionality into the incorporated nitrogen dopants. This phenomenon might suggest that the transformation of surface amino groups into nitrogen dopants falls within the temperature range of 600−800 ℃.[7]

Temperature-oriented Decomposition of Nitrogen Dopants. TG analysis under nitrogen environment was adopted to further verify the observed gradient change of nitrogenous contents under different temperature ranges (**Figure 1a**). The transcending mass decay (calculated by subtracting the mass loss of the background DBC) of the BMDBC at 600 ℃ was 1.7 *wt.*% while those for NBC500-800 were all around 0.8 *wt.*%, corroborating the temperature-oriented transformation of labile nitrogen contents.[41] For the temperature ranging between 600 and 800 ℃, the difference in mass decay of the BMDBC further increased to 2.2 *wt.*%, which indicated that the nitrogenous dopants proceeded to decompose within this temperature range. Compared with the NBC500 and NBC600 with a transcending mass decay of 1.3 *wt.*% and 0.5 *wt.*%, respectively,

those for the NBC700 and NBC800 showed only slight differences from the background, which implied that the decomposition of pyrrolic and pyridinic N should occur below 700 ℃. The transcending mass decay at 1000 ℃ was employed to estimate the graphitic N level in the NBC700 (0.3 *wt.*%), while the TG curve of the NBC800 almost overlapped with the background, indicating a complete decomposition of nitrogen dopants at 800 ℃. The decomposition feature of graphitic N in NBC (700−800 ℃) was similar to the cleavage of sp^2-hybridized carbon-nitrogen bonding in carbon nitride (740 ℃). It is likely that the formation of electroactive nitrogen vacancies, which are commonly observed in carbon nitride after the fission of sp^2-hybridized C−N, might also occur within NBC. In terms of XRD patterns for biochars (**Figure S6**), the exothermic peak at ~625 ℃ in the DTG stemmed from the decarbonation of calcite, a common ash content in lignocellulosic biomass, which showed nearly no decay difference among biochars and exhibited no reactivity in the catalytic reaction.

The N 1s XPS spectra were evaluated to further explore the compositional distribution of nitrogen dopants (**Figure 1b**, **Figure S7**, and **Table S2**). The transformation of nitrogen species was found to display a sequential order, *i.e.*, the amino groups dominated when the annealing temperature was lower than 600 ℃ before its transformation into pyrrolic N and pyridinic N between 600-700 ℃, then graphitic N took over as the main nitrogen species when the temperature was increased to 700 ℃, and finally a complete decomposition of nitrogen dopants at 800 ℃ (as illustrated by the proposed transformation scheme in **Figure S8**). This might indicate the gradual and temperature-oriented evolution of nitrogen dopants into nitrogen vacancies. With respect to the C 1s and O 1s spectra, two critical indicators were extracted to reveal the changes of surface chemistry on NBCs. The graphitization degree (C=C/C−C, **Figure S9**) suggested a positive linear relationship with the increase of annealing temperature, while the carbonylation degree (C=O/C−O,

Figure S10) showed a notable elevation when annealing temperature was escalated to 800 ℃. This appealing scenario might imply that the dopant decomposition also caused the interspecies transformation of the C=O/C−O, which could be accompanied with the generation of hydroquinone-type persistent free radicals (PFRs) as the intermediate product.[42] Both the well-developed graphitized carbon matrix and the evolvement of the PFRs were regarded as crucial factors for the nonradical activation of PMS.[43-47]

Evolution of Nitrogen Vacancies. The surface lattice disorder of the NBCs was inspected using non-destructive Raman depth scanning with a penetrative depth of 0.8 nm.[48] Raman curves were deconvoluted into several characteristic peaks, *i.e.*, S band at 1290 cm^{-1} assigned to the transformation of sp^2- to sp^3-hybridization in carbon lattice, D band at 1350 cm^{-1} assigned to the defective and disorder arrangement of carbon atoms, V1 band at 1520 cm^{-1} assigned to the amorphous carbon and deterioration of crystallinity, V2 band at 1545 cm^{-1} assigned to the semicircle ring breathing, G1 band at 1590 cm^{-1} assigned to sp^2-hybridized aromatics with 3-5 rings, and G2 band at 1620 cm^{-1} assigned to the highly ordered sp^2-hybridized aromatics.[26, 49, 50] The detailed information obtained from the deconvolution is summarized in **Table S3** and **Figure S11**.

Typical indictor, namely A_D/A_G, was first employed to illustrate the change of defective degree on the biochar surface. As the nitrogen dopants are energetically preferable to substitute carbon atoms at the edges,[13] their decomposition is likely to increase the structural disorder and correspondingly promote the increase of defective level. The decomposition of nitrogen dopants positively correlated with the density of defects owing to the formation of nitrogen vacancies (**Table S3**). The A_D/A_G value maintained at ~0.40 in most of the biochars while the NBC800 showed a distinct depth distribution from the others (**Figure S9f**). Accordingly, the curves assigned

to surface (NBC800-surface) and below 0.8 nm (NBC800-0.8) were separately deconvoluted. The NBC800-surface showed a higher A_D/A_G value of 1.82 than that of the NBC800-0.8 at 0.73, indicating that the surface of the NBC800 was enriched with more defects than its inner structure. The nature of these defects was elaborated using an indicator (A_D/A_V) with 3.5 as the borderline value.[50] The carbons with an A_D/A_V value higher than 3.5 was perceived to possess more vacancies as the dominant defects, while the ones with a lower A_D/A_V value were supposed to contain a higher density of boundary edges.[51] The surface of the NBC800 was primarily dominated by vacancies with an A_D/A_V value of 6.01, which was higher than others ranging from 0.26−1.57. All the above results corroborated the evolvement of nitrogen vacancies from dopant decomposition in NBC800.

Impact of Dopant Decomposition on Graphitic Structure. Another indicator A_{G1}/A_{G2} was adopted to further describe the disorder level of sp^2-hybridized carbons, which corresponds to the ratio between randomly organized and well-condensed carbon units. The original DBC and NBC500-700 possessed a high A_{G1}/A_{G2} value, probably resulting from the nonstoichiometric nature of biochar matrices. Intriguingly, the constitutive arrangement of carbon units on the NBC800 surface was highly ordered with an A_{G1}/A_{G2} value of 0.72 lower than 2.92 for NBC800-0.8 (**Figure 2a** and **Figure S9g**). This phenomenon might indicate that the nitrogen vacancies, unlike armchair or zig-zag defects which cause carbon disorders, would not disrupt the graphitic integrity.

Compared with the TEM images of the original DBC, BMDBC, and NBC500-700 (**Figure S12**), the NBC800 demonstrated a distinctive graphitic morphology, consisting of lattice fringe at 0.25 nm assigned to the stacking of graphite layers, with many graphitic nanosheets distributed over the carbon surface (**Figure 2b**).[9] The TEM images of another three nitrogen-doped carbons (*i.e.*, NAC,

NG, and NCNTs) were also obtained for direct comparison. Graphitic nanosheets on the NBC800 was more similar to those on the NAC, although the density of graphitic nanosheets on the NBC800 was much greater.

Catalytic Performance of the NBCs. Catalytic activities of the NBCs were evaluated using PMS, which possesses an asymmetric structure susceptible to nonradical activation, as the oxidant in the degradation of 4-chlorophenol (4-CH, $pH_a = 9.41$). The obtained experimental data were fitted using the pseudo-first-order model (**Figure S13**). The addition of PMS alone could not decompose 4-CH (**Figure 3a**, less than 2%). The addition of DBC only elevated the removal rate to 9.1% while 8.1% of the 4-CH could be adsorbed in the absence of PMS, suggesting a weak catalytic ability of the unmodified DBC. Although CO_2 activation can create a small amount of carbon vacancies on DBC, its trivial catalytic capacity implied that the mere carbon vacancies without any cooperation with other electroactive components could not anchor the peroxide molecules, which was in a good agreement with our recent findings.[26] Conventional NBC derived from the direct thermal treatment of DBC with urea also demonstrated poor catalytic performance (less than 20%), probably because the nitrogen dopants can easily release under the high-temperature environment due to the nonstoichiometric nature of CO_2-activated carbon matrices.[52]

After the wet ball milling to introduce amino groups, an increase in adsorption capacity of the BMDBC towards 4-CH (**Figure 3b**, 18.7%) was observed owing to a higher density of basic sites on the biochar surface, but the catalytic performance was still unfavorable (20.8%). With temperature-oriented annealing to tune the nitrogen dopants, the NBC500 (adsorption 9.3%, overall removal 12.4%) and NBC600 (adsorption 11.7%, overall removal 16.3%) exhibited marginal promotion, while the NBC700 (adsorption 32.5%, overall removal 61.4%) and NBC800 (adsorption 38.7%, overall removal 90.9%) showed a remarkably improved performance in the 4-

CH degradation. Considering that the SSA range of NBCs (from 353 to 395 m^2 g^{-1}) was comparable to that of the starting biochar DBC (366 m^2 g^{-1}), its small influence might be offset by the formation of nitrogen vacancies under an increasing temperature which played the major roles in the carbocatalysis.

Impact of Dimensional Structure Properties. The SSA and A_{G1}/A_{G2} were evaluated to investigate whether the structure properties influenced the availability of active sites. Results show that the increase of SSA could be positively correlated with the adsorption/removal ratio, confirming that the SSA prompted the process of organic adsorption as expected. However, a negative relationship could be found between the values of SSA and k_{obs}, suggesting that another temperature-dependent property governed the availability of catalytic sites over SSA (**Figure 3c**). The relationship between the A_{G1}/A_{G2} ratio and kinetic data is plotted in **Figure 3d**, in which representative carbons with different dimensional structures and their nitrogen-doped materials were studied for comparison. No obvious correlation could be constructed between various carbocatalysts, while the carbons with an A_{G1}/A_{G2} ratio lower than ~2 (*i.e.*, NBC700, NBC800, CNTs, and NCNTs) manifested a much stronger promotion on both the removal rate and k_{obs}. Those nitrogen-doped carbons that underwent temperature-oriented annealing and possessed less labile nitrogen contents displayed a lower A_{G1}/A_{G2} in contrast to their starting materials. Previous studies have reported that the heteroatoms doping can significantly promote the graphitization of carbons due to the sp^2-hybridization nature of nitrogen dopants,[2, 18] while it is interesting to reveal in this study that the introduction of nitrogen vacancies would not disrupt the graphitic structure.

Although the NAC and NBC800 possessed a similar 3D structure, their catalytic performance differed to a large extent. Compared with the NAC with low removal rate and k_{obs} (40.6%, 0.011 min^{-1}), more efficient catalytic degradation could be reached for the NBC800 (90.9%, 0.0375

337 min^{-1}) with considerable 2.25- and 3.26-fold increases, respectively. The GR was selected as a
338 highly graphitized 2.5D carbon material with scarce defects and oxygen-moieties on the surface.[53]
339 Both the GR and NGR showed trivial contribution (less than 15%) to the carbocatalysis, implying
340 that the intact sp^2-hybridization structure merely displayed an electroneutral feature with a low
341 reactivity.[1, 9] Basically, the main difference between the NBC800 and NGR/NAC lies in the
342 refractory surface oxygen contents, which determine the surface hydrophilicity and facilitate
343 subsequent interaction with organics dissolved in the aqueous phase. With respect to the 1D CNTs-
344 based material, Ren et al. employed electrochemical technique to unravel the electron transfer
345 regime on the NCNTs during the PMS activation for phenols oxidation, and highlighted the critical
346 role of nonradical surface-confined metastable complex.[16, 32]

347 **Substrate Specificity.** Given that phenols with various functionalities possess disparate
348 electrochemical potentials,[54] substrate specificity analysis based on different phenolic structures
349 was conducted to explore the redox mechanisms and the potential involvement of surface-confined
350 metastable PMS complex. The phenol (PH), hydroquinone (HQ), 4-CH, and 4-nitrophenol (4-NP)
351 correspond to the phenolic structures connected with one or two electron-donating groups (−OH),
352 an attached halogen atom that may scavenge radicals (−Cl), and an electron-withdrawing group
353 ($-NO_2$), respectively (**Table S4**). Only the NBC700 and NBC800 that represented the NBCs
354 functionalized with graphitic N and nitrogen dopants, respectively, were selected to proceed the
355 substrate specificity test. As shown in **Figure S14**, both the NBC700 and NBC800 demonstrated
356 higher selectivity towards those phenols functionalized with electron-donating groups. The PH and
357 HQ could be easily removed following an order of NBC800 (92.6% and 88.3%) > NCNTs (91.2%
358 and 86.1%) > NBC700 (68.6% and 78.1%) > CNTs (63.6% and 42.1%). It was reported that the
359 PH and HQ are prone to donate electrons in the electron-transfer regime, while the 4-NP shows

chemical reluctance to be oxidized.[32] Both the NBC700 (13.4%) and NBC800 (34.4%) demonstrated much weaker catalytic performance in regard to the 4-NP remediation. This phenomenon was similar to the catalytic behavior of the CNTs and NCNTs which followed a nonradical pathway in the 4-NP degradation, indicating a similar nonradical feature under the catalysis of nitrogen vacancies.

Redox Behavior in the Carbocatalysis. The mineralization degree of the 4-CH was evaluated, as high as ~90% of the TOC could be removed in the NBC800/PMS system, while that of the NCNTs was significantly lower (76.7%) although it showed a better removal rate and k_{obs} than the NBC800 in the kinetics study (**Figure S15**). This scenario might illustrate the preponderance of NBC800 over the NCNTs in the organics removal, as low-dimensional materials are generally regarded to possess fewer hierarchical porous tunnels and less adsorptive sites to retain organics.[31]

The amount of released chloride during the catalytic reaction was also monitored to investigate the conversion of 4-CH (**Figure 4a**). Both the CNTs (30.3 mg L^{-1}) and NCTs (35.3 mg L^{-1}) showed a higher Cl^- release than those for the NBC700 (16.9 mg L^{-1}) and NBC800 (22.7 mg L^{-1}), which might be ascribed to the anion-π interaction with NBC that mitigated the ion release into the aqueous solution.[55] The smaller amount of released Cl^- was conducive to the catalytic reaction as Cl^- would scavenge the surface ROS (**eqs. 1** and **2**).[3]

$$Cl^- + \cdot OH = \cdot Cl + OH^-, k = 4.3 \times 10^9\ M^{-1}s^{-1} \quad (1)$$

$$Cl^- + \cdot SO_4^- = \cdot Cl + SO_4^{2-}, k = 3.1 \times 10^8\ M^{-1}s^{-1} \quad (2)$$

The attenuation trend of the PMS against time is plotted in **Figure 4a**. The NBC700 and CNTs consumed less than 1.0 mM PMS, which was consistent with their catalytic performance. Compared with the NBC800 with a similar catalytic activity, the NCNTs proceeding the catalytic reaction through a nonradical pathway consumed more PMS in the 4-CH degradation (1.24 mM

383 *vs.* 1.55 mM). Strong organics degradation with a low consumption of peroxide is a characteristic
384 feature for nonradical carbocatalysis.[56] The nonradical pathway is more sustainable as it only
385 targets at reacting with electron-rich organics and consumes less PMS molecules with minimal
386 interference from the other background constituents (*i.e.*, pH, background ions, water molecules)
387 and/or self-scavenging effects.[2] Lower PMS consumption of the NBC800 might suggest a different
388 nonradical pathway based on the nitrogen vacancies in contrast to the electron transfer regime
389 reported on the NCNTs.

390 **Superior PMS Affinity of Nitrogen Vacancies.** The PMS adsorption capacities of the NBCs
391 and CNTs after 30- and 180-min mixing were measured to probe their affinity towards the PMS
392 at the initial and equilibrium stages (**Figure S16**), which could reflect the density of active sites
393 throughout the biochar matrices. Both the DBC and CNTs showed a limited PMS adsorption in
394 the absence of nitrogen doping, and the PMS adsorption predominantly happened in the initial
395 stage. A linear correlation could be constructed with respect to the annealing temperature, which
396 was related to the temperature-oriented transformation of nitrogen dopants. The NBC800 (0.432
397 mM) exhibited a nearly identical equilibrium PMS adsorption amount to that of the NCNTs (0.429
398 mM), suggesting that the affinity of nitrogen-doped biochar towards PMS played a key role in
399 nonradical carbocatalysis.

400 The equilibrium PMS adsorptive capacity was further correlated with point of zero charge (pH_{pzc},
401 **Figure S17**) and k_{obs} to explore the underlying interaction (**Figure 4b**). It was concluded that the
402 PMS adsorption mainly depended on the electrostatic force, as reflected by a good linear
403 relationship with the pH_{pzc} values of NBCs. A low equilibrium PMS adsorptive capacity below 0.2
404 mM marginally initiated the catalytic degradation (grey region), while the higher catalytic
405 capacities of the NBC700 and NBC800 could be attributed to their stronger affinities towards the

406 PMS (0.285 and 0.432 mM). The two-stage pattern might be caused by the varied PMS affinities
407 of different nitrogen species. Under the temperature range below 600 ℃, the dominating nitrogen
408 species were pyrrolic N and pyridinic N, which probably possess lower PMS adsorption energies.[57]
409 Under a higher temperature range over 700 ℃, the evolved graphitic N dominated and enhanced
410 the affinity of adjacent carbon atom to attract negatively-charged PMS molecules, while the
411 vacancies were likely to harbor negative PMS molecules due to the creation of positive holes.[58]
412 The PMS adsorption amount could positively correlate with the formation and reactivity of the
413 metastable complex.[16] Nevertheless, the NAC with the highest equilibrium PMS adsorption of
414 0.739 mM showed an inferior catalytic performance. This might suggest that a good affinity
415 towards the PMS on the high-dimensional carbons is not the only prerequisite to prompt the
416 nonradical degradation.

417 **Nature of Surface Complex on Nitrogen Vacancies.** EPR spectrometer was employed to
418 measure the G factors which can signify the density of polarized unpaired electrons possessing a
419 paramagnetic feature (**Figure 5a**). The characteristic peak intensity for the DBC could be barely
420 detected, while those for the NBCs continuously increased with the temperature. The
421 decomposition of electron-rich nitrogen dopants led to a delocalized electron distribution towards
422 the adjacent atoms, and a positive nitrogen vacancy could be generated to interact with the negative
423 PMS anions. A good correlation was found between the equilibrium PMS adsorptive capacity and
424 the G factors of the NBCs, suggesting that the PMS affinity was also associated with the surface
425 PFRs categories. The g factors for the NBC700 and NBC800 were 2.0025 and 2.0021, respectively,
426 which were lower than 2.0038 of the NBC500 and 2.0031 of the NBC600 (**Table S5**). The carbon-
427 centered PFRs (Landé factor range: 2.0020-2.0030) in NBC700 and NBC800 converted from the
428 oxygenated carbon-centered PFRs (Landé factor range: 2.0030-2.0040) in NBC500 and

NBC600,[59] and exhibited a higher activity in the PMS accumulation promoting the formation of surface complex. The oxygenated carbon-centered PFRs may also contribute to the formation of surface complex on the nitrogen vacancies, as evidenced by the C=C/C−C indicator obtained in the XPS analysis. The pH values of the NBC700/PMS and NBC800/PMS systems notably dropped from 6.0 ±0.2 to 3.2 ±0.4 after the PMS addition, suggesting that the formation of surface complex accompanied with the release of protons.

In-situ Raman spectra of the NBCs were analyzed to understand the nature of surface-confined complexes (**Figure 5b**). Four characteristic peaks at approximately 835, 880 or 1071, and 978 cm^{-1} correspond to the metastable surface-confined complex ($*HSO_5^-$), the PMS molecules (HSO_5^-), and the sulphate ions (HSO_4^-), respectively. The peak areas assigned to $*HSO_5^-$ were calculated and plotted against k_{obs} in the 4-CH degradation. The suspension was mixed for 30 s before the launch of 532 nm laser and the scanning was faster than the normal spectrum acquisition. Thus, the intensity of $*HSO_5^-$ was primarily controlled by the availability of nitrogen vacancies on the surface of NBCs. The k_{obs} values were found to have a good linear relationship ($R^2 = 0.98$) with the calculated peak areas for $*HSO_5^-$, corroborating that the nitrogen vacancies accounted for the formation of surface-confined $*HSO_5^-$ to boost the nonradical degradation.

Typical chemicals, ethanol (EtOH), *tert*-butanol (TBA), and NaN_3, were selected as the radical scavengers to differentiate the types of the surface-confined ROS in the representative NBC800/PMS system (*i.e.*, $^{\bullet}OH$, $^{\bullet}SO_4^-$, and $^1O_2$) (**Figure S18**). The EtOH could promptly quench all the ROS on carbon surface or in bulk solution, while the TBA and NaN_3 selectively reacted with mere $^{\bullet}OH$ and $^1O_2$ released in solution, respectively (**Table S6**). Results indicate that the participation of EtOH significantly impeded the 4-CH degradation while TBA and NaN_3 displayed only limited scavenging effects. These results may provide an additional evidence that the surface-

confined ROS should account for the 4-CH degradation, demonstrating its nonradical feature in the NBC-based carbocatalysis without relying on free radicals. It should be remarked that the addition of alcoholic scavengers can drastically affect the adsorption capacities of high-dimensional carbons towards organics and peroxides, not to mention that NaN_3 directly consumes the PMS molecules at a high dosage.[2, 60] Therefore, the results from scavenger experiments can only serve as a qualitative proof in the mechanistic study. The EPR spectra were obtained using the DMPO and TEMP as the spin trapping agents. Weak signals assigned to all the ROS could be detected (**Figures S19** and **S20**). Previous studies have raised concerns over the spin trapping agents which are extremely susceptible to the ROS in aqueous phase.[3] The results in this study may also indicate that they could not serve as a valid evidence for the ROS formed at the liquid-carbon interface. Misleading information from the scavenger experiments and EPR spectrometer might be responsible for the inconsistent interpretation in the biochar studies, especially in the presence of nonradical surface complex.[1]

Proposed Formation Pathway of Surface Complex. Overall, the plausible carbocatalysis mechanisms in the PMS activation for the NBCs can be unveiled. With respect to the commonly reported active sites (graphitic N), the nitrogen dopants could generate a dipole moment (electronegativity, $\chi_C = 2.55 < \chi_N = 3.04$) with the positively-charged adjacent carbon atom to bind with the negative PMS anion, and the negatively-charged nitrogen center as the electron donor to cleave the peroxide bond *via* an electron transfer process (**eq. 3**).[61] However, this process is usually low in efficiency due to the generation of by-product peroxymonosulfate anion radicals ($^{\bullet}SO_5^-$) with a moderate oxidizing power.[2] As evidenced in the Raman and XPS analyses, the decomposition of nitrogen dopants could lead to the formation of positive nitrogen vacancies with a polarized electron distribution over the adjacent atoms to create respective PFRs. Consequently,

the newly formed carbon-centered PFRs (major fraction, **eq. 4**) and the oxygenated carbon-centered PFRs (minor fraction, **eq. 5**) attracted PMS anion to induce the generation of metastable surface-confined complex $*HSO_5^-$ through a hydrogen abstraction process, which could facilitate a high-efficiency carbocatalysis. This catalytic pathway is basically nonradical with a low consumption of the PMS molecules.

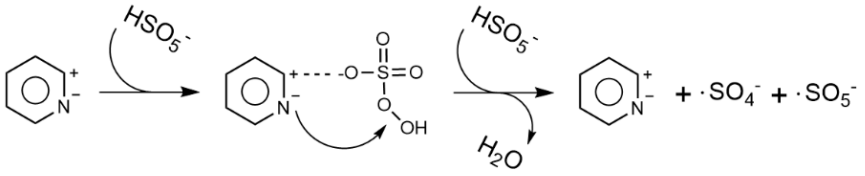

(3)

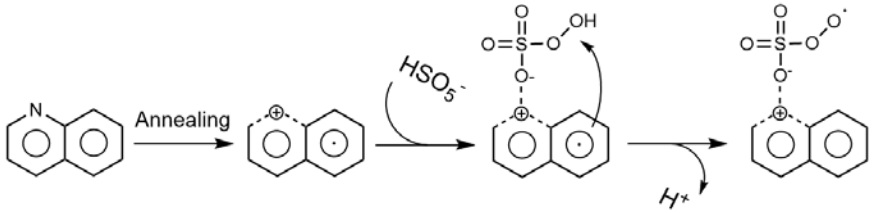

(4)

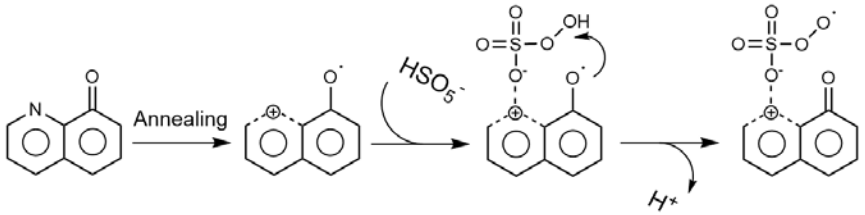

(5)

Durability and Reusability. To evaluate the durability of nitrogen vacancy, the NBC800 was subjected to the natural aging process. Only a slight discrepancy of the 4-CH catalytic degradation was observed between the aged and fresh NBC800 (87.4% *vs.* 90.9%, **Figure S21**). EPR spectra indicated that the aged NBC800 possessed a higher G factor than that of the fresh NBC800 (2.0026 *vs.* 2.0021, **Figure S22**), suggesting that the carbon-centered PFRs partly transformed into their oxygenated state due to natural rainfall and atmospheric oxidation. Although its EPR intensity moderately decreased after natural aging, it seems that the PMS affinity of nitrogen vacancy was

marginally influenced (0.401 mM *vs.* 0.432 mM, **Figure S23**), whereas the PMS adsorptive capacity of aged NBC800 deviated from the linear correlation constructed among NBCs. Therefore, the natural aging process introduced oxygen contents but hardly attenuated the nitrogen vacancy and its adjacent carbon-centered PFRs. This phenomenon also signified the chemical perseverance of nitrogen vacancy and its electroactive selectivity to specified nucleophiles. Given that the conventional electron-donating PFRs (*e.g.*, oxygen-centered type) are unstable under synthetic procedure (> 700 °C) and natural conditions,[20, 42, 62] nitrogen vacancy on biochar can promise good flexibility to cater for the industry-specific operational conditions in practical applications.

The recyclability and regeneration tests were also carried out (**Figure S21**). The results showed that the catalytic capacities of the spent NBC800 dropped to 54.1% in the 2nd run and 29.6% in the 3rd run. The thermal annealing treatment could remediate its efficacy to 54.8%, comparable to that in the 2nd run. This might suggest that some of the nitrogen vacancies and adjacent PFRs were irreversibly consumed in the 1st run, whereas the regenerative hybrid structures including edging sites, oxygen functionalities, and sp^2-hybridized basal planes accounted for the remaining carbocatalysis.[58] While the formation of nitrogen vacancy can offer durable and flexible features, the deactivation mechanisms and regeneration of heteroatoms still require further evaluation in practical conditions.

Treatment of Simulated Phenolic Wastewater. Seven types of simulated phenolic wastewater were configured and Types I, II, and III were indicative of the industrial wastewater containing single, multiple, and total kinds of phenols, respectively (**Table S7**). In Types I-1 to I-4 with respective phenolic components, their TOC and BOD degradation rates followed a similar pattern to those in the substrate-specific study, where Type II-4 containing 4-NP showed the lowest removal efficiencies (TOC: 18.7%, COD: 41.8%). Regarding the individual removal of each

phenol (**Figure S25**), there was only a minor drop by 14.8% in the 4-CH degradation while its TOC degradation rate declined by 40.6%. By comparing the trends in Types II and III, the involvement of electron-deficient 4-NP showed a restrained efficiency for nitrogen vacancy based carbocatalysis. These results indicated that the coexisting components in the simulated phenolic wastewater compromised to some extent the formation of surface-bound complexes, hence the mineralization extent and toxicological analysis might require future investigation.

It is noted that over 70% of the inorganic carbon contents (CO_3^{2-} and HCO_3^-) was detained within the biochar matrices when single phenolic component was involved (Type I), whereas a high strength of phenolic compounds (Types II and III) occupied the active sites and led to a lower inorganics removal in the range of 16.8-22.1% (**Figure S24**), indicative of the higher affinity of phenolic compounds over background ions. In addition, all types of the simulated wastewater were originally non-biodegradable with the BOD/COD ratios lower than 0.02,[63] while their BOD/COD ratios displayed a 26- to 105-fold improvement after the nitrogen vacancy based carbocatalysis, which shows a good prospect to be integrated with other wastewater treatment units.

Environmental Implications. In this work, we proposed and implemented a hypothesis-driven manipulation over the design of NBCs to rule out the interferences from the other redox-active components on the original biochar matrices. Herein, mechanistic formation of nonradical surface complex on the NBCs was elaborated. The decomposition of introduced nitrogen dopants was found to create reactive nitrogen vacancies, which had been overlooked in the existing literatures. Further EPR and *in-situ* Raman analyses uncovered that the PFRs (*i.e.*, carbon-centered and oxygenated carbon-centered types) adjacent to the nitrogen vacancies might be the essential active sites of the NBCs. The formation of surface-bound complexes was determined by the hydrogen abstraction process rather than the conventional electron transfer. The reaction rate coefficient in

the carbocatalysis was primarily governed by PMS adsorptive capacities of the NBCs, which were in alignment with the densities of the nitrogen vacancies and PFRs formed on the graphitic units. Nonradical carbocatalysis based on the nitrogen vacancies of graphitic biochar exhibited comparable efficacy to that of the commercial NCNTs-based system. Furthermore, the nitrogen vacancy based carbocatalysis showed both good flexibility and catalytic performance in the remediation of simulated phenolic wastewater. Overall, we believe that the unveiling of catalytic mechanisms in the economical and environmentally benign NBC system could deliver more fit-for-purpose solutions towards sustainable and practical industrial wastewater treatment.

ASSOCIATED CONTENT

Supporting Information. Information about the used chemicals. Detailed procedures to the involved characterizations (SEM, TEM, Raman, XPS, EPR, *etc*.) and the analytical measurements of organics (TC, COD, BOD, *etc*.). Curves of the organic degradation and the PMS adsorption. Supplementary tables and figures about the material morphology, elements, catalysis, practical applications, *etc*.

ACKNOWLEDGEMENT

The authors appreciate the financial support from the Hong Kong Research Grants Council (PolyU 15217818 and PolyU 15222020) and PolyU Project of Strategic Importance. The support from the University Research Facility on Chemical and Environmental Analysis (UCEA) of PolyU is also gratefully acknowledged.

REFERENCES

(1) Wan, Z.; Sun, Y.; Tsang, D. C. W.; Hou, D.; Cao, X.; Zhang, S.; Gao, B.; Ok, Y. S., Sustainable remediation with electroactive biochar system: Mechanisms and perspectives. *Green Chem.* **2020,** *22*, 2688-2711.

(2) Oh, W.-D.; Lim, T.-T., Design and application of heterogeneous catalysts as peroxydisulfate activator for organics removal: An overview. *Chem. Eng. J.* **2019,** *358*, 110-133.

(3) Lee, J.; von Gunten, U.; Kim, J.-H., Persulfate-based advanced oxidation: Critical assessment of opportunities and roadblocks. *Environ. Sci. Technol.* **2020,** *54*, (6), 3064-3081.

(4) Wan, Z.; Cho, D.-W.; Tsang, D. C. W.; Li, M.; Sun, T.; Verpoort, F., Concurrent adsorption and micro-electrolysis of Cr(VI) by nanoscale zerovalent iron/biochar/Ca-alginate composite. *Environ. Pollut.* **2019,** *247*, 410-420.

(5) Zhang, T.; Chen, Y.; Wang, Y.; Le Roux, J.; Yang, Y.; Croue, J. P., Efficient peroxydisulfate activation process not relying on sulfate radical generation for water pollutant degradation. *Environ. Sci. Technol.* **2014,** *48*, (10), 5868-75.

(6) Zhu, S.; Li, X.; Kang, J.; Duan, X.; Wang, S., Persulfate activation on crystallographic manganese oxides: Mechanism of singlet oxygen evolution for nonradical selective degradation of aqueous contaminants. *Environ. Sci. Technol.* **2019,** *53*, (1), 307-315.

(7) Duan, X.; Sun, H.; Wang, S., Metal-free carbocatalysis in advanced oxidation reactions. *Acc. Chem. Res.* **2018,** *51*, (3), 678.

(8) Ortiz-Medina, J.; Wang, Z.; Cruz-Silva, R.; Morelos-Gomez, A.; Wang, F.; Yao, X.; Terrones, M.; Endo, M., Defect engineering and surface functionalization of nanocarbons for metal-free catalysis. *Adv. Mater.* **2019,** *31*, (13), 1805717.

(9) Chen, X.; Duan, X.; Oh, W.-D.; Zhang, P.-H.; Guan, C.-T.; Zhu, Y.-A.; Lim, T.-T., Insights into nitrogen and boron-co-doped graphene toward high-performance peroxymonosulfate

582 activation: Maneuverable N-B bonding configurations and oxidation pathways. *Appl. Catal. B:*
583 *Environ.* **2019,** *253*, 419-432.
584 (10) Duan, X.; O'Donnell, K.; Sun, H.; Wang, Y.; Wang, S., Sulfur and nitrogen co-doped
585 graphene for metal-free catalytic oxidation reactions. *Small* **2015,** *11*, (25), 3036-3044.
586 (11) Duan, X.; Ao, Z.; Sun, H.; Zhou, L.; Wang, G.; Wang, S., Insights into N-doping in single-
587 walled carbon nanotubes for enhanced activation of superoxides: a mechanistic study. *Chem.*
588 *Comm.* **2015,** *51*, (83), 15249-15252.
589 (12) Xing, B.; Dong, J.; Yang, G.; Jiang, N.; Liu, X.; Yuan, J. J. A. C. A. G., An insight into N,
590 S-codoped activated carbon for the catalytic persulfate oxidation of organic pollutions in water:
591 Effect of surface functionalization. *Appl. Catal. A: Gen.* **2020,** *602*, 117714.
592 (13) Yang, Q.; Xiao, Z.; Kong, D.; Zhang, T.; Duan, X.; Zhou, S.; Niu, Y.; Shen, Y.; Sun, H.;
593 Wang, S.; Zhi, L., New insight to the role of edges and heteroatoms in nanocarbons for oxygen
594 reduction reaction. *Nano Energy* **2019,** *66*, 104096.
595 (14) Gao, K.; Wang, B.; Tao, L.; Cunning, B. V.; Zhang, Z.; Wang, S.; Ruoff, R. S.; Qu, L.,
596 Efficient metal-free electrocatalysts from N-doped carbon nanomaterials: Mono-doping and co-
597 doping. *Adv. Mater.* **2019,** *31*, (13), 1805121.
598 (15) Wan, Z.; Sun, Y.; Tsang, D. C. W.; Khan, E.; Yip, A. C. K.; Ng, Y. H.; Rinklebe, J.; Ok,
599 Y. S., Customised fabrication of nitrogen-doped biochar for environmental and energy
600 applications. *Chem. Eng. J.* **2020,** *401*, 126136.
601 (16) Ren, W.; Nie, G.; Zhou, P.; Zhang, H.; Duan, X.; Wang, S., The intrinsic nature of
602 persulfate activation and N-doping in carbocatalysis. *Environ. Sci. Technol.* **2020,** *54*, (10), 6438-
603 6447.
604 (17) Wang, H.; Guo, W.; Liu, B.; Si, Q.; Luo, H.; Zhao, Q.; Ren, N., Sludge-derived biochar as

605 efficient persulfate activators: Sulfurization-induced electronic structure modulation and disparate
606 nonradical mechanisms. *Appl. Catal. B: Environ.* **2020,** *279*, 119361.
607 (18) Wang, H.; Guo, W.; Liu, B.; Wu, Q.; Luo, H.; Zhao, Q.; Si, Q.; Sseguya, F.; Ren, N., Edge-
608 nitrogenated biochar for efficient peroxydisulfate activation: An electron transfer mechanism.
609 *Water Res.* **2019,** *160*, 405-414.
610 (19) Wan, Z.; Sun, Y.; Tsang, D. C. W.; Xu, Z.; Khan, E.; Liu, S.-H.; Cao, X., Sustainable
611 impact of tartaric acid as electron shuttle on hierarchical iron-incorporated biochar. *Chem. Eng. J.*
612 **2020,** *395*, 125138.
613 (20) Zhu, S.; Huang, X.; Ma, F.; Wang, L.; Duan, X.; Wang, S., Catalytic removal of aqueous
614 contaminants on N-doped graphitic biochars: Inherent roles of adsorption and nonradical
615 mechanisms. *Environ. Sci. Technol.* **2018,** *52*, (15), 8649-8658.
616 (21) Ho, S.-H.; Chen, Y.-d.; Li, R.; Zhang, C.; Ge, Y.; Cao, G.; Ma, M.; Duan, X.; Wang, S.;
617 Ren, N.-q., N-doped graphitic biochars from C-phycocyanin extracted Spirulina residue for
618 catalytic persulfate activation toward nonradical disinfection and organic oxidation. *Water Res.*
619 **2019,** *159*, 77-86.
620 (22) Ding, D.; Yang, S.; Qian, X.; Chen, L.; Cai, T., Nitrogen-doping positively whilst sulfur-
621 doping negatively affect the catalytic activity of biochar for the degradation of organic contaminant.
622 *Appl. Catal. B: Environ.* **2020,** *263*, 118348.
623 (23) Jiang, H.; Gu, J.; Zheng, X.; Liu, M.; Qiu, X.; Wang, L.; Li, W.; Chen, Z.; Ji, X.; Li, J.,
624 Defect-rich and ultrathin N doped carbon nanosheets as advanced trifunctional metal-free
625 electrocatalysts for the ORR, OER and HER. *Energ. Environ. Sci.* **2019,** *12*, (1), 322-333.
626 (24) Jia, Y.; Zhang, L.; Du, A.; Gao, G.; Chen, J.; Yan, X.; Brown, C. L.; Yao, X., Defect
627 graphene as a trifunctional catalyst for electrochemical reactions. *Adv. Mater.* **2016,** *28*, (43), 9532-

9538.

(25) Wang, J.; Duan, X.; Gao, J.; Shen, Y.; Feng, X.; Yu, Z.; Tan, X.; Liu, S.; Wang, S., Roles of structure defect, oxygen groups and heteroatom doping on carbon in nonradical oxidation of water contaminants. *Water Res.* **2020,** *185*, 116244.

(26) Wan, Z.; Sun, Y.; Tsang, D. C. W.; Yu, I. K. M.; Fan, J.; Clark, J. H.; Zhou, Y.; Cao, X.; Gao, B.; Ok, Y. S., A sustainable biochar catalyst synergized with copper heteroatoms and CO_2 for singlet oxygenation and electron transfer routes. *Green Chem.* **2019,** *21*, (17), 4800-4814.

(27) Ding, J.; Xu, W.; Wan, H.; Yuan, D.; Chen, C.; Wang, L.; Guan, G.; Dai, W.-L., Nitrogen vacancy engineered graphitic C_3N_4-based polymers for photocatalytic oxidation of aromatic alcohols to aldehydes. *Appl. Catal. B: Environ.* **2018,** *221*, 626-634.

(28) Hong, Z.; Shen, B.; Chen, Y.; Lin, B.; Gao, B., Enhancement of photocatalytic H_2 evolution over nitrogen-deficient graphitic carbon nitride. *J. Mater. Chem. A* **2013,** *1*, (38), 11754-11761.

(29) Sun, C.; Chen, T.; Huang, Q.; Zhan, M.; Li, X.; Yan, J., Activation of persulfate by CO_2-activated biochar for improved phenolic pollutant degradation: Performance and mechanism. *Chem. Eng. J.* **2020,** *380*, 122519.

(30) Xu, X.; Zheng, Y.; Gao, B.; Cao, X., N-doped biochar synthesized by a facile ball-milling method for enhanced sorption of CO_2 and reactive red. *Chem. Eng. J.* **2019,** *368*, 564-572.

(31) Duan, X.; Sun, H.; Jian, K.; Wang, Y.; Wang, S., Insights into heterogeneous catalysis of persulfate activation on dimensional-structured nanocarbons. *ACS Catal.* **2015,** *5*, (8), 4629-4636.

(32) Ren, W.; Xiong, L.; Yuan, X.; Yu, Z.; Zhang, H.; Duan, X.; Wang, S., Activation of peroxydisulfate on carbon nanotubes: Electron-transfer mechanism. *Environ. Sci. Technol.* **2019,** *53*, (24), 14595-14603.

(33) Wang, L.; Chen, L.; Tsang, D. C. W.; Kua, H. W.; Yang, J.; Ok, Y. S.; Ding, S.; Hou, D.;

651 Poon, C. S., The roles of biochar as green admixture for sediment-based construction products.
652 *Cem. Concr. Compos.* **2019,** *104*, 103348.
653 (34) Sun, X.; Wang, C.; Li, Y.; Wang, W.; Wei, J., Treatment of phenolic wastewater by
654 combined UF and NF/RO processes. *Desalination* **2015,** *355*, 68-74.
655 (35) Su, X.; Wang, Y.; Xue, B.; Hashmi, M. Z.; Lin, H.; Chen, J.; Wang, Z.; Mei, R.; Sun, F.,
656 Impact of resuscitation promoting factor (Rpf) in membrane bioreactor treating high-saline
657 phenolic wastewater: Performance robustness and Rpf-responsive bacterial populations. *Chem.*
658 *Eng. J.* **2019,** *357*, 715-723.
659 (36) Tian, H.; Xu, X.; Qu, J.; Li, H.; Hu, Y.; Huang, L.; He, W.; Li, B., Biodegradation of
660 phenolic compounds in high saline wastewater by biofilms adhering on aerated membranes. *J.*
661 *Hazard. Mater.* **2020,** *392*, 122463.
662 (37) Pan, F.; Cao, Z.; Zhao, Q.; Liang, H.; Zhang, J., Nitrogen-doped porous carbon nanosheets
663 made from biomass as highly active electrocatalyst for oxygen reduction reaction. *J. Power*
664 *Sources* **2014,** *272*, 8-15.
665 (38) Lyu, H.; Gao, B.; He, F.; Zimmerman, A. R.; Ding, C.; Tang, J.; Crittenden, J. C.,
666 Experimental and modeling investigations of ball-milled biochar for the removal of aqueous
667 methylene blue. *Chem. Eng. J.* **2018,** *335*, 110-119.
668 (39) Lyu, H.; Gao, B.; He, F.; Zimmerman, A. R.; Ding, C.; Huang, H.; Tang, J., Effects of ball
669 milling on the physicochemical and sorptive properties of biochar: Experimental observations and
670 governing mechanisms. *Environ. Pollut.* **2018,** *233*, 54-63.
671 (40) Duan, X.; Ao, Z.; Zhou, L.; Sun, H.; Wang, G.; Wang, S., Occurrence of radical and
672 nonradical pathways from carbocatalysts for aqueous and nonaqueous catalytic oxidation. *Appl.*
673 *Catal. B: Environ.* **2016,** *188*, 98-105.

(41) Kundu, S.; Xia, W.; Busser, W.; Becker, M.; Schmidt, D. A.; Havenith, M.; Muhler, M., The formation of nitrogen-containing functional groups on carbon nanotube surfaces: a quantitative XPS and TPD study. *PCCP* **2010,** *12*, (17), 4351-4359.

(42) Zhong, D.; Jiang, Y.; Zhao, Z.; Wang, L.; Chen, J.; Ren, S.; Liu, Z.; Zhang, Y.; Tsang, D. C. W.; Crittenden, J. C., pH dependence of arsenic oxidation by rice-husk-derived biochar: Roles of redox-active moieties. *Environ. Sci. Technol.* **2019,** *53*, (15), 9034-9044.

(43) Zhu, S.; Huang, X.; Yang, X.; Peng, P.; Li, Z.; Jin, C., Enhanced transformation of Cr(VI) by heterocyclic-N within nitrogen-doped biochar: Impact of surface modulatory persistent free radicals (PFRs). *Environ. Sci. Technol.* **2020,** *54*, (13), 8123-8132.

(44) Duan, X.; Sun, H.; Ao, Z.; Zhou, L.; Wang, G.; Wang, S., Unveiling the active sites of graphene-catalyzed peroxymonosulfate activation. *Carbon* **2016,** *107*, 371-378.

(45) Sun, H.; Liu, S.; Zhou, G.; Ang, H. M.; Tadé, M. O.; Wang, S., Reduced graphene oxide for catalytic oxidation of aqueous organic pollutants. *ACS Appl. Mater. Inter.* **2012,** *4*, (10), 5466-5471.

(46) Wang, Y.; Ao, Z.; Sun, H.; Duan, X.; Wang, S., Activation of peroxymonosulfate by carbonaceous oxygen groups: experimental and density functional theory calculations. *Appl. Catal. B: Environ.* **2016,** *198*, 295-302.

(47) Oh, W.-D.; Lisak, G.; Webster, R. D.; Liang, Y.-N.; Veksha, A.; Giannis, A.; Moo, J. G. S.; Lim, J.-W.; Lim, T.-T., Insights into the thermolytic transformation of lignocellulosic biomass waste to redox-active carbocatalyst: Durability of surface active sites. *Appl. Catal. B: Environ.* **2018,** *233*, 120-129.

(48)Pérez, L. A.; Bajales, N.; Lacconi, G. I., Raman spectroscopy coupled with AFM scan head: A versatile combination for tailoring graphene oxide/reduced graphene oxide hybrid materials.

697 *Appl. Surf. Sci.* **2019,** *495*, 143539.
698 (49) Yang, X.; Igalavithana, A. D.; Oh, S. E.; Nam, H.; Zhang, M.; Wang, C. H.; Kwon, E. E.;
699 Tsang, D. C. W.; Ok, Y. S., Characterization of bioenergy biochar and its utilization for
700 metal/metalloid immobilization in contaminated soil. *Sci. Total Environ.* **2018,** *640-641*, 704-713.
701 (50) Yang, Q.; Chen, Y.; Duan, X.; Zhou, S.; Niu, Y.; Sun, H.; Zhi, L.; Wang, S., Unzipping
702 carbon nanotubes to nanoribbons for revealing the mechanism of nonradical oxidation by
703 carbocatalysis. *Appl. Catal. B: Environ.* **2020,** *276*, 119146.
704 (51) Eckmann, A.; Felten, A.; Mishchenko, A.; Britnell, L.; Krupke, R.; Novoselov, K. S.;
705 Casiraghi, C., Probing the nature of defects in graphene by Raman spectroscopy. *Nano Lett.* **2012,**
706 *12*, (8), 3925-3930.
707 (52) Wu, D.; Song, W.; Chen, L.; Duan, X.; Xia, Q.; Fan, X.; Li, Y.; Zhang, F.; Peng, W.; Wang,
708 S., High-performance porous graphene from synergetic nitrogen doping and physical activation
709 for advanced nonradical oxidation. *J. Hazard. Mater.* **2020,** *381*, 121010.
710 (53) Xu, Z.; Xu, X.; Tao, X.; Yao, C.; Tsang, D. C. W.; Cao, X., Interaction with low molecular
711 weight organic acids affects the electron shuttling of biochar for Cr(VI) reduction. *J. Hazard.*
712 *Mater.* **2019,** *378*, 120705.
713 (54) Steenken, S.; Neta, P., One-electron redox potentials of phenols. Hydroxy-and
714 aminophenols and related compounds of biological interest. *J. Phys. Chem.* **1982,** *86*, (18), 3661-
715 3667.
716 (55) Schottel, B. L.; Chifotides, H. T.; Dunbar, K. R., Anion-π interactions. *Chem. Soc. Rev.*
717 **2008,** *37*, (1), 68-83.
718 (56) Zhong, Q.; Lin, Q.; Huang, R.; Fu, H.; Zhang, X.; Luo, H.; Xiao, R., Oxidative degradation
719 of tetracycline using persulfate activated by N and Cu codoped biochar. *Chem. Eng. J.* **2020,** *380*,

720 122608.

721 (57) Wang, G.; Chen, S.; Quan, X.; Yu, H.; Zhang, Y., Enhanced activation of
722 peroxymonosulfate by nitrogen doped porous carbon for effective removal of organic pollutants.
723 *Carbon* **2017,** *115*, 730-739.

724 (58) Duan, X.; Li, W.; Ao, Z.; Kang, J.; Tian, W.; Zhang, H.; Ho, S.-H.; Sun, H.; Wang, S.,
725 Origins of boron catalysis in peroxymonosulfate activation and advanced oxidation. *J. Mater.*
726 *Chem. A* **2019,** *7*, (41), 23904-23913.

727 (59) Odinga, E. S.; Waigi, M. G.; Gudda, F. O.; Wang, J.; Yang, B.; Hu, X.; Li, S.; Gao, Y.,
728 Occurrence, formation, environmental fate and risks of environmentally persistent free radicals in
729 biochars. *Environ. Int.* **2020,** *134*, 105172.

730 (60) Yun, E. T.; Lee, J. H.; Kim, J.; Park, H. D.; Lee, J., Identifying the Nonradical Mechanism
731 in the Peroxymonosulfate Activation Process: Singlet Oxygenation Versus Mediated Electron
732 Transfer. *Environ. Sci. Technol.* **2018,** *52*, (12), 7032-7042.

733 (61) Duan, X.; Indrawirawan, S.; Kang, J.; Tian, W.; Zhang, H.; Duan, X.; Zhou, X.; Sun, H.;
734 Wang, S., Synergy of carbocatalytic and heat activation of persulfate for evolution of reactive
735 radicals toward metal-free oxidation. *Catal. Today* **2019**.

736 (62) Ruan, X.; Sun, Y.; Du, W.; Tang, Y.; Liu, Q.; Zhang, Z.; Doherty, W.; Frost, R. L.; Qian,
737 G.; Tsang, D. C. W., Formation, characteristics, and applications of environmentally persistent
738 free radicals in biochars: A review. *Bioresour. Technol.* **2019,** *281*, 457-468.

739 (63) Samudro, G.; Mangkoedihardjo, S., Review on BOD, COD and BOD/COD ratio: A
740 triangle zone for toxic, biodegradable and stable levels. *Int. J. Acad. Res.* **2010,** *2*, (4).